Journal of The Electrochemical Society, **161** (3) A422-A430 (2014)
0013-4651/2014/161(3)/A422/9/$31.00 © The Electrochemical Society

Particle Size Polydispersity in Li-Ion Batteries

Ding-Wen Chung,[a,*] Paul R. Shearing,[b] Nigel P. Brandon,[c] Stephen J. Harris,[d,] and R. Edwin García[a,z]**

[a]*School of Materials Engineering, Purdue University, West Lafayette, Indiana, USA*
[b]*Department of Chemical Engineering, University College London, London, United Kingdom*
[c]*Department of Earth Science and Engineering, Imperial College London, London, United Kingdom*
[d]*Lawrence Berkeley National Laboratory, Berkeley, California, USA*

Starting from three-dimensional X-ray tomography data of a commercial $LiMn_2O_4$ battery electrode, the effect of microstructure on the electrochemical and chemo-mechanical response of lithium-ion batteries is analyzed. Simulations show that particle size polydispersity impact the local chemical and electrical behavior of a porous electrode, while particle-particle mechanical interactions favor intercalation induced stress accumulation, resulting in a mechanically unreliable electrode microstructure. Simulations based on computer-generated electrode microstructures demonstrate that broad particle size distributions deliver up to two times higher energy density than monodisperse-sized particles based electrodes for low C-rates. However, monodisperse particle size distribution electrodes deliver the highest energy and power density for high discharge rates due to a higher surface area of reactive material per unit volume. Calculations show that the surface roughness in experimentally determined electrodes is 2.5 times higher than the one delivered by perfectly smooth spherical particles in computer generated electrodes, and provide high instantaneous power performance, but accelerate side reactions that impact negatively on power performance. The combined experimental and modeling approach demonstrates that porous electrodes with spatially uniform microstructural features improve electrochemical performance and mechanical reliability, especially for high power density applications.
 [DOI: 10.1149/2.097403jes]

Manuscript submitted June 20, 2013; revised manuscript received December 30, 2013. Published January 15, 2014.

Advances in materials chemistry, processing techniques, and electrode microstructure have delivered great advances in rechargeable lithium-ion battery technology. These accomplishments enable the possibility to substitute or complement conventional gasoline-based technologies with hybrid and full electric vehicles.[1] However, technological challenges such as poor cycle life and low power performance arise from material limitations and the absence of advanced microstructural engineering.[2] Traditionally, in commercially used electrodes, microstructural properties such as porosity, average particle size, and electrode thickness have been used to specify the microstructural characteristics to minimize the macroscopic power density limitations. Recent work, however, has demonstrated that by engineering the electrode microstructure, significant performance enhancement can be achieved.[3-8] In particular, advanced particle morphological engineering,[9] particle packing and polydispersity and its impact on the local tortuosity,[10] and particle surface chemistry and roughness,[11] have demonstrated its importance to maximize charge capacity and device reliability.

Experimentally, Shearing, Kehrwald, Brandon, and Harris pioneered the use of X-ray tomography to characterize the porosity and tortuosity uniformity of graphite composite electrode microstructures.[12-14] Wheeler and coworkers used focused ion beam-scanning electron microscopy (FIB-SEM) to extract microstructural cross sections of $LiCoO_2$ electrodes and predict the macroscopic transport properties.[15] Ender, Hutzenlaub, and coworkers further employed FIB-SEM to three-dimensionally reconstruct battery electrodes and calculate its porosity, specific surface area, and pore connectivity.[16,17] In addition, Wilson and Harris combined FIB-SEM and EBSD to image the crack and multi-grained particles in $LiCoO_2$ electrodes.[18] Most recently, Chung, Ebner, García, and Wood utilized X-ray tomography to identify individual particles and correlate macroscopic microstructural properties to processing variables such as electrode compression and carbon black weight percent, and found that particle packing inhomogeneities lead to an undesired increase in tortuosity.[11,19]

In contrast, modeling and simulation approaches pioneered by Doyle, Newman, and many others incorporated mean-field descriptions that utilize *averaged* microstructural features to provide quantitative insight on lithium-ion battery cell design.[20-32] García and coworkers integrated SEM and Finite Element simulations to spatially resolve the effects microstructure on the local electrochemical kinetics.[5,33,34] Sastry et al. showed that particle packing and morphology impact the average transport behavior and macroscopic mechanical deformation in porous electrodes.[35-37] Recently, Zhu, Kee et al. employed mean-field descriptions and applied them to simulate the electrochemical performance of battery electrode in three-dimensional reconstructed microstructures.[38,39]

In spite of the great deal of work, understanding of the microstructural characteristics has focused on the average performance of battery electrodes with an emphasis on the impact of porosity on the tortuosity inhomogeneities in the electrodes. While such work is key to understanding the impact of processing on important parameters, it fails to capture its effect on the local electrochemical interactions and its associated inhomogeneities.

In this paper, starting from X-ray tomography data of a $LiMn_2O_4$ electrode microstructure (see Figure 1), the effect of particle size polydispersity and surface roughness are quantified and assessed in the context of realizing dramatically improved designs. In particular, effect of particle size polydispersity on the local electrochemical interactions in lithium-ion battery electrodes are rationalized through the use of computer-generated electrode microstructures. Here, the influence of the particle size distribution for both low and high discharge rates is numerically quantified to rationalize the results obtained by using three-dimensional, experimentally determined sections. Optimal particle size distributions as a function of C-rate are proposed.

Theoretical Framework

Electrochemical kinetics.— For a lithium-ion battery system composed of active material and electrolyte, mass and charge transport is described by the set of partial differential equations:[40]

$$\frac{\partial c}{\partial t} = \nabla \cdot D\nabla c + \nabla \cdot L\nabla\phi \qquad [1]$$

$$\frac{\partial \rho}{\partial t} = \nabla \cdot \sigma\nabla\phi + \nabla \cdot L\nabla c \qquad [2]$$

as proposed and throughly validated by García and others.[5,33,34,41] c is the local concentration of lithium, D is the lithium diffusivity, ρ is the electrical charge accumulation, σ is the electrical conductivity, ϕ is the electrostatic potential, and t is time. L is the electromigration coefficient, $L = DzFc/RT$, where z is the valence charge of lithium,

*Electrochemical Society Student Member.
**Electrochemical Society Active Member.
zE-mail: redwing@purdue.edu

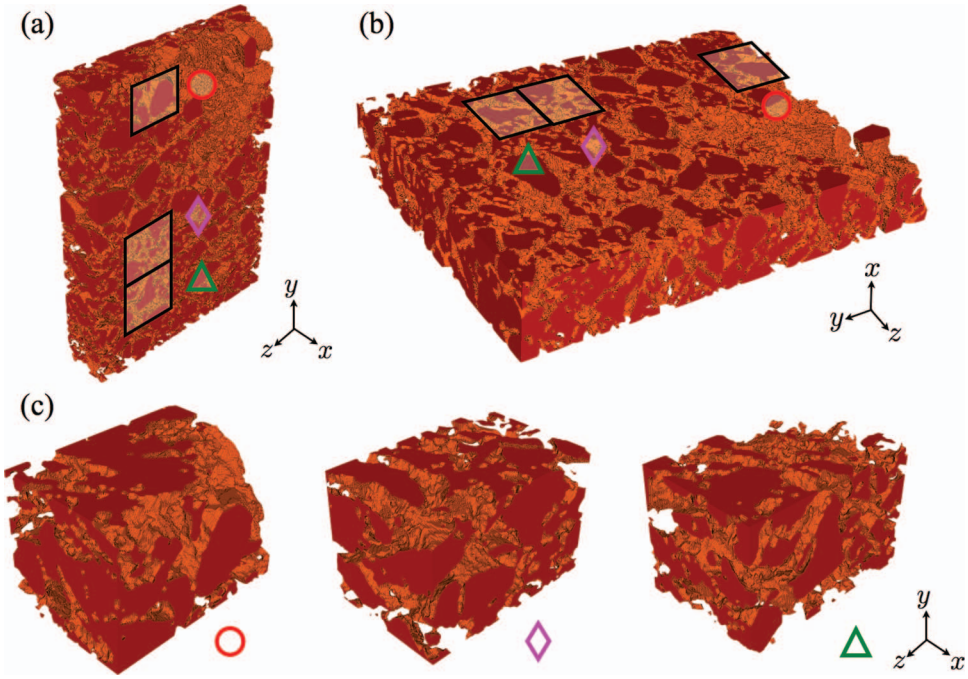

Figure 1. (a) (b) Three-dimensional rendering of X-ray tomography reconstructed $LiMn_2O_4$ electrode from a commercial lithium-ion battery. The reconstructed, 60 μm × 360 μm × 270 μm, electrode exhibits a porosity of $\epsilon = 0.4$. Large spatial variations of porosity are observed in the experimental electrode. (c) Individual tomogram, 60 μm × 60 μm × 90 μm, sections (◯: $\epsilon = 0.29$; ◇: $\epsilon = 0.45$; △: $\epsilon = 0.40$) used for electrochemical and chemo-mechanical analysis demonstrate that local variations in roughness, particle size, and packing impact the macroscopic electrochemical response.

F is Faraday's constant, R is the gas constant, and T is the absolute temperature. Equation 1 corresponds to a modified expression of Fick's first and second law and Equation 2 corresponds to Kirchoff's law in its differential form. Equations 1 and 2 reduce to the classical diffusion and charge continuity equations in the limit of $z = 0$.

Lithium intercalation occurs at the electrode-electrolyte interface, i.e., $Li^+ + e^- \rightleftharpoons Li$. The rate of reaction is controlled by the local overpotential, η, as given by the Butler-Volmer relation:[42]

$$\vec{J} \cdot \hat{n} = i_\circ (e^{\frac{\alpha_a F \eta}{RT}} - e^{-\frac{\alpha_c F \eta}{RT}}) \quad [3]$$

The first term on the right side of Equation 3 corresponds to the forward rate of the anodic process and the second term corresponds to the backward rate of the reaction. Here, α_a and α_c are the forward and reversed intercalation empirical constants. The surface reaction is further dependent on the exchange current density, $i_\circ$, which has the form:

$$i_\circ = F k_r (c_s - c)^{\alpha_a} c^{\alpha_c} \quad [4]$$

k_r is the electrochemical reaction rate constant and c_s is the lithium solubility limit.

Mechanical equilibrium.— During galvanostatic cycling, intercalation compounds experience significant volumetric changes, and mechanical stress distribution develops in the battery. The equilibrium stress state is resolved through the mechanical equilibrium equation:

$$\nabla \cdot \overleftrightarrow{\sigma} = \vec{0} \quad [5]$$

To describe the chemo-mechanical state of the system, Hooke's law is recast as:[34,43]

$$\sigma_{ij} = C_{ijkl}\left[\varepsilon^T_{kl} - \beta_{kl}(c - c_\circ)\right] \quad [6]$$

where C_{ijkl} is the elastic stiffness tensor, β_{kl} is the Vegard tensor, $c_\circ$ is the stress free concentration and ε^T_{kl} is the total geometrical strain.

Average microstructural properties.— Macroscopically, the reactivity of the active material is determined by the available surface area per unit volume. A higher area density corresponds to a greater instantaneous power performance because the active material layer can intercalate more lithium ions per unit volume in the absence of active material transport limitations. Fundamentally, the theoretical description of the effect of area density on battery electrodes is summarized through the well established porous electrode theory.[21] For an electrode composed of perfectly spherical active material particles, the area density, a, is given by $a = 3(1 - \epsilon)/\bar{r}$, where ϵ is the porosity of the electrode and $\bar{r}$ is the average particle radius. In practice, particle surface roughness allows an electrode layer to achieve a higher area density,[11] i.e.,

$$a = \frac{3(1 - \epsilon) S_A}{\bar{r}} \quad [7]$$

where S_A is the average surface roughness of the electrode. Here, S_A is defined as the surface area ratio of a representative roughened particle to the surface area of a perfectly smooth and spherical particle. Thus, for an electrode composed of perfectly smooth particles, $S_A = 1$, and $S_A > 1$ as the surface roughness increases.

Experimental

The $LiMn_2O_4$ electrode was supplied by E1 Moli where fragments of the electrode were easily separated from the aluminum foil without the requirement for chemical dissolution (as described by Shearing et al. in Ref. 12). The X-ray diffraction of the electrode structure is matched by the ICDD database to $LiMn_2O_4$.

Micro-XRM experiments have been conducted using the 150 kV Xradia MicroXCT-200 at the Henry Moseley X-ray Imaging Facility at the University of Manchester, UK. Using a white X-ray beam, images were captured across a −91 to 91 degree angular range with 20 second exposure. The resulting transmission images were reconstructed using the Xradia XRM Reconstructor software suite, resulting in an imaged volume $> 1 \times 10^7$ μm^3 with corresponding voxel sizes of 597nm. Image analysis and binarization of the resulting tomographic

Table I. Discrete Element Method Simulation parameters.[34,52] A Hooke's law contact model with a damping contribution was used to describe both the normal and tangential contact mechanics of particles during compaction.

Name	Value	Units
Damping coefficient	1.81×10^{-5}	-
Density of active particles	4750	kg/m^3
Dynamic coefficient of friction	0.15	-
Poisson ratio of active particles	0.3	-
Static coefficient of friction	0.25	-
Young's modulus of active particles	200	GPa
Young's modulus of compaction wall	180	GPa

volume has been carried out using the Avizo Fire software package (see Shearing et al. in Ref. 13).

It is noteworthy that higher resolution scans of the same electrode material have also been conducted using laboratory and synchrotron nano-CT instruments: as may be expected the higher resolution scans revealed an increase in volume specific surface area, however the porosity and pore connectivity were observed to be approximately constant between the different techniques. This suggests that the resolution requirement to characterize the bulk pore structure is not as stringent as for surface area studies and in this case, lower resolution can be tolerated without sacrificing data quality while simultaneously leveraging the statistical advantages of larger analysis volumes.

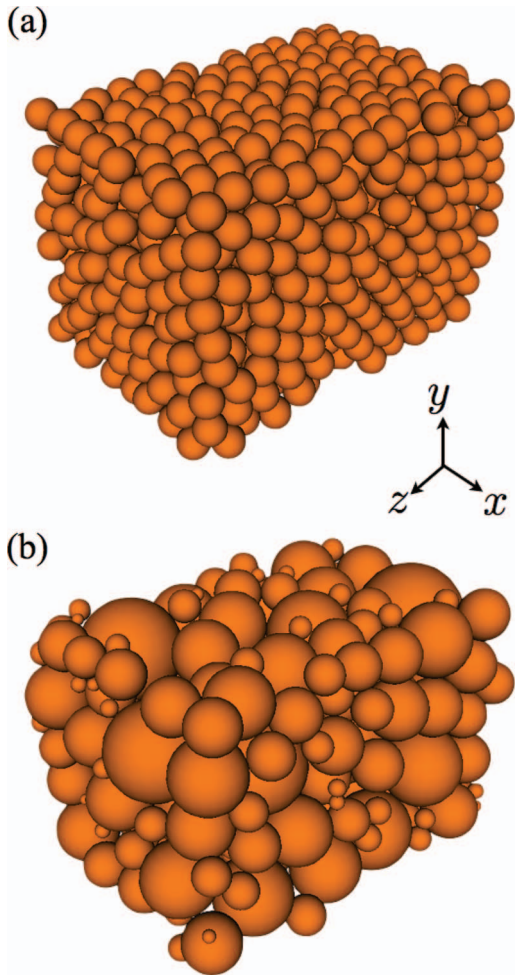

Figure 2. Example computer-generated microstructures produced through Discrete Element Modeling.[45] (a) corresponds to monodisperse distribution, $\sigma_r = 0$, and (b) corresponds to a polydisperse distribution, $\sigma_r = \bar{r}$. The porosity is $\epsilon = 0.35$. Physical dimensions of simulated electrodes are 60 μm × 60 μm × 90 μm.

Numerical Setup

Numerical representations of porous electrode microstructures were generated by inserting spherical particles with defined radii drawn from a size distribution with a polydispersity, σ_r, into a simulation domain. The electrode was compacted to a specified porosity through a Discrete Element Method (DEM) package, ESyS-Particle,[45] where the normal and rotational particle contact mechanics were defined through Hooke's law with a damping factor model. Utilized DEM simulation parameters are summarized in Table I.

Figure 2 shows a set of example DEM-generated electrodes. Here, calculations were performed with a fixed porosity of, $\epsilon = 0.35$. The particle size was set to match a Gaussian distribution with an average particle radius of $\bar{r}$ =3 μm, and a polydispersity of $\sigma_r = 0$ for monodisperse electrodes and $\sigma_r = \bar{r}$ for polydisperse electrodes.

The local electrochemical response for both experimentally reconstructed and computer-generated electrodes was simulated by implementing Equations 1 to 6 in Batts3D.[46] A 12 μm separator layer was added to the side of the electrode facing the $+x$ axis. Meshes on the order of 120 × 100 × 150 elements resulted in linear systems of equations with approximately 1.8×10^6 degrees of freedom. Utilized material properties and simulation parameters are summarized in Table II. Meshes were fragmented into individual domains, each of them embodying a single material phase. A constant current density was applied at the current collector on the face parallel to the $-x$ plane of the simulation domain. The separator at the $+x$ face was electrically grounded. Chemically, a fixed concentration boundary condition, $c = 0.1c_s$, was applied at the separator face. Mechanically, the three-dimensional simulation domain was free from applied external forces, i.e., not subjected to external constraints. The resultant system of equations were solved using a relative tolerance of 1×10^{-4}. Each electrochemical simulation used on the order to 80 GB of memory and took approximately 50 hours of wall time on an eight core, 128 GB random access memory (RAM), 2.4 GHz Linux Ubuntu 10.04 server.

Table II. Physical Properties used in $LiMn_2O_4$ battery half cell simulations.[34,52-54]

Symbol	Name	Value	Units
D_c	Lithium diffusivity in $LiMn_2O_4$	1×10^{-13}	m^2/s
D_e	Lithium diffusivity in electrolyte	1×10^{-9}	m^2/s
E_c	Young's modulus of $LiMn_2O_4$	200	GPa
E_e	Young's modulus of electrolyte	1	MPa
R_c	Electrode contact resistance	1.5×10^{-3}	Ω
k_c	Reaction rate constant at $LiMn_2O_4$ | electrolyte interface	1.1×10^{-10}	m/s
c_T	Normalization concentration value for lithium	2.29×10^{4}	mol/m^3
${c_i}^c$	Normalized initial concentration of lithium in cathode	0.1	–
$\bar{r}$	Average particle radius	3×10^{-6}	m
α_c	Anodic empirical constant	0.5	–
α_a	Cathodic empirical constant	0.5	–
β	Vegard coefficient of $LiMn_2O_4$	0.016	–
σ_c	Electrical conductivity of $LiMn_2O_4$	3.8	S/m
σ_e	Electrical conductivity of electrolyte/carbon mixture	2.53	S/m

The chemo-mechanical simulations required on the order of 30 GB of RAM and 30 hours of wall time to converge.

The volume fraction populations of active material that has been utilized during the discharge sequence was summarized in terms of a frequency plot (histogram), where each position-dependent concentration value displays a time-dependent likelihood of occurring. The bin size, k, was selected to be 300, in agreement with the non-parametric density estimation method proposed by Izeman where $k = 1/2\sigma N^{(-1/3)} \approx 300$.[47]

Results and Discussion

Experimentally reconstructed microstructures.— Upon reconstruction, the experimentally obtained $LiMn_2O_4$ electrode exhibits significant particle size, porosity, and spatial homogeneity variations (see Figure 1). The electrode exhibits a macroscopic porosity of $\epsilon = 0.4$, an average particle size of $\bar{r}$ =7 μm, and a surface roughness of $S_A = 2.49$. Because the intercalation kinetics and parasitic reactions in lithium-ion batteries are highly sensitive to the available surface area density, deviations from $S_A = 1$ suggest that adjustments need to be made on porous electrode theory to accommodate the effect of particle morphology on the performance and reliability of battery electrodes. Moreover, for the microstructure analyzed herein, the surface roughness enhances the instantaneous power density of the electrode. However, its local inhomogeneities also impact on power density reliability and will ultimately lead to poor material utilization, as discussed below.

Individual sections in Figure 1(c) further demonstrate variations in local microstructural properties of the reconstructed electrode. For the extracted sections, porosity ranges from $\epsilon = 0.29$ to $\epsilon = 0.45$, and surface roughness ranges from $S_A = 2.26$ to $S_A = 3.33$. In particular, Figure 3(a) shows interconnected particles which in turn induce a set of connected mesoporous channels. The naturally occurring polydispersity of the particles results in spatial nonuniformity in active material packing, mainly integrated of clusters of small particles.

Figure 3(b) shows the normalized lithium concentration distribution at the end of a 1C discharge, and shows that local mesoporous channels facilitate lithium intercalation.[48] Moreover, regions populated with small particle clusters show a great degree of lithium accumulation. In contrast, the slow solid state diffusion and low surface area density from regions occupied by large particles display a significantly lower lithium concentration accumulation.

Figure 3(c) shows the corresponding voltage field at the end of discharge. Similar to the concentration, voltage is highly inhomogeneous due to the spatial variation in particle packing and particle size across the electrode. Regions rich with small particle clusters favor faster capacity utilization while regions with larger particles favor low utilization of charge due to its low available exposed area to the electrolyte per unit volume.

Figure 4 shows the spatial distribution of the discharge and charging stresses after a 1C galvanostatic cycle. The intensity of the intercalation induced stress is quantified through the first stress invariant, i.e., the hydrostatic stress. Here, the mechanical displacement

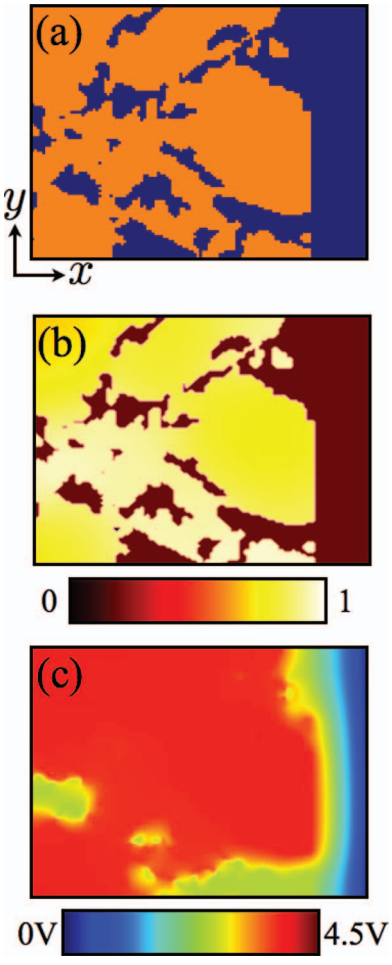

Figure 3. (a) Microstructure cross section of a three-dimensional tomogram section, ◯, as shown in Figure 1(c). The concentration (b) and voltage (c) at the end of a 1C galvanostatic discharge demonstrate significant local performance inhomogeneities that correlate to microstructural properties.

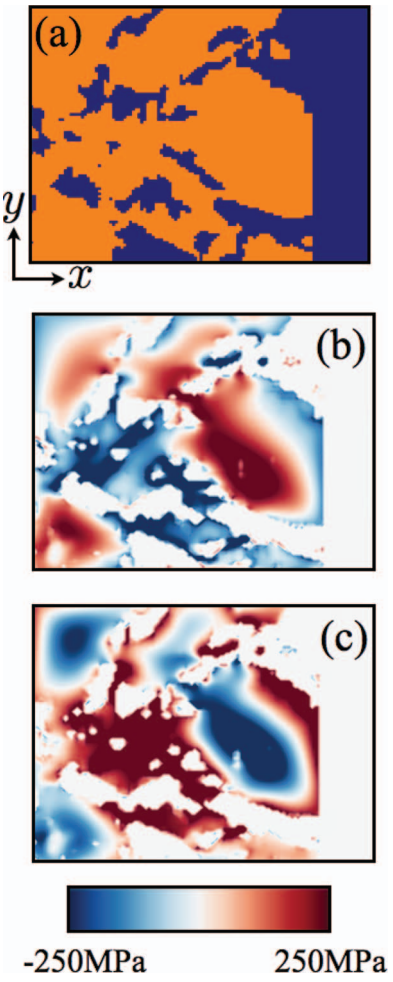

Figure 4. (a) Microstructure cross section of a tomogram section ◯. Spatially resolved first stress invariant at the end of a 1C discharge (b) and a recharge (c) process demonstrate interlocking of particles prevents the stress distribution to relax, resulting in mechanical failure of active material.

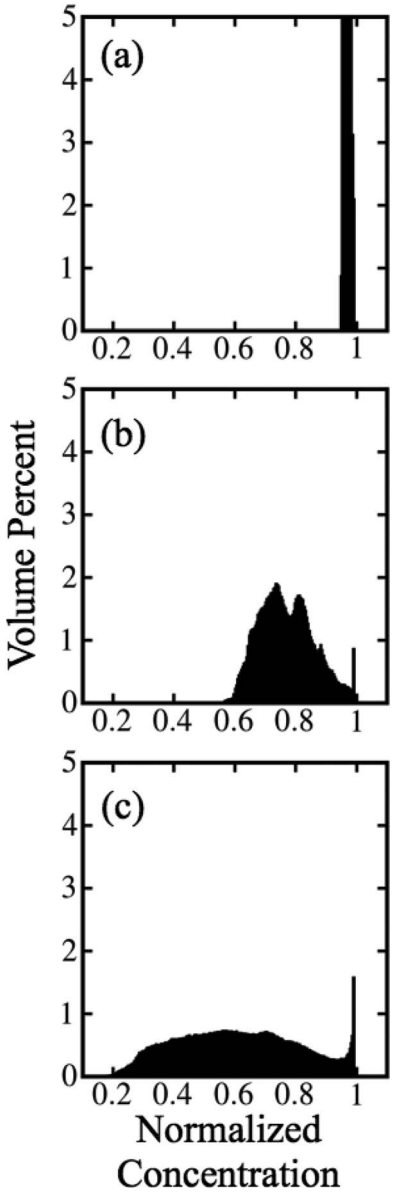

Figure 5. Lithium concentration distribution histogram of the reconstructed microstructure at the end of (a) 1/5C, (b) 1C, and (c) 5C discharge. The concentration distribution shows that a significant fraction of the theoretical charge capacity is not utilized at high C-rates due to an unoptimized active material size polydispersity.

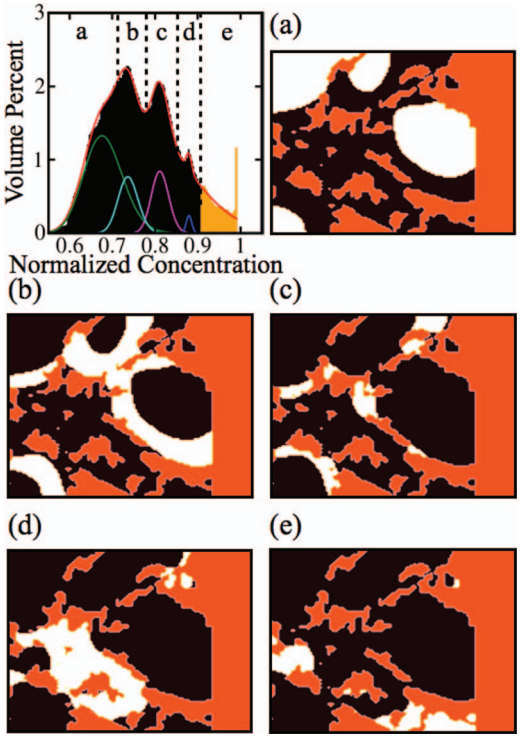

Figure 6. Heterogeneous lithium accumulation populations visualization. Insets (a) through (e) show regions of active material with increasing lithium concentration. Each white area highlights the microstructural feature that contributes to concentration distribution subpopulation in the histogram.

caused by the electrode filler, i.e., polymer binder, is negligible because of its associated small elastic moduli, thus only the active material volumetric changes contribute toward the elastic stress and enables additional mechanical relaxation during galvanostatic cycling. During discharge, the volume occupied by small particle clusters exhibits a compressive stress while larger particles experience a tensile stress as a result of the steep concentration gradients that develop on those regions that are electrochemically isolated. The mechanical stress state is reversed during a recharge process. In addition, surface roughness and closed porosity further intensify the local stress. In particular, high surface roughness leads to a higher degree of stress from the increased local electrochemically active surface area. In contrast, closed porosity simultaneously favors mechanical fracture and capacity losses in lithium-ion battery electrodes because dense electrochemically isolated regions tend to be in a tensile state during discharge, which in turn become favorable locations for crack propagation because the isolated porosity area acts as stress concentrators.[49-51] Current results demonstrate that interparticle connectivity in the simulated reconstructed microstructures prevents stress relaxation thus favoring mechanical failure. Hence, particle adhesion and interlocking suppress the reliability and will accelerate mechanical failure.[52] However, if interparticle shearing or grain boundary sliding occurred, the local stress intensity would be reduced.

The effect of discharge rate on the local lithium concentration accumulation is quantified in Figure 5. For low discharge rates, e.g., 1/5C, the microstructure has no appreciable effect on the local lithium accumulation, as expected. At moderate discharge rates, e.g., 1C, the local microstructure inhomogeneities split the lithium concentration into multiple microstructural populations. Each lithium concentration population is a result of specific microstructural features and result in different electrochemical states (see Figure 6). Furthermore, the large particle size polydispersity of the commercial battery microstructure suggests that a significant fraction of active material becomes unutilized as the discharge rate increases. For high discharge rates, e.g., 5C, the inhomogeneous lithium distribution leads to a dramatic broadening in the concentration histogram (see Figure 5(c)). Specifically, regions that accumulate a greater amount of lithium correspond to locations in the electrode with a greater exposed area per unit volume, namely clusters of small particles, where lithium can be rapidly replenished, such as those internal pores that directly connect to the separator. Regions with low lithium concentration correspond to the core of particles, or electrochemically shielded regions.

Figure 7 shows the macroscopic voltage of the half-cell system as a function of utilized charge of the three selected electrode sections, shown in Figure 1. Simulations demonstrate a higher *useful* capacity with decreasing porosity. Here, section ◯ surpasses the delivered capacity of section △ by over 60% while its porosity is only 37% lower. Moreover, the used capacity of section ◊ exceeds the capacity of section △ by 10% even though the electrode porosity is lower by 13%. While this further supports results such as those reported by Smith et al.[5] on the effect of microstructural properties, it also highlights that particle size polydispersity, and local electrode reactivity play a critical role in specifying the macroscopic energy density.

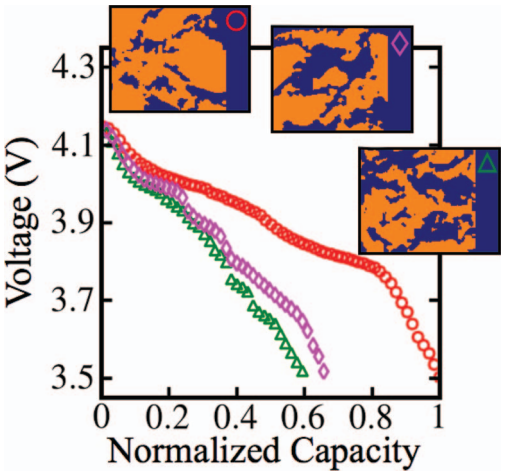

Figure 7. 1C voltage vs. capacity curves for electrode for different porosity values, ϵ (◯: $\epsilon = 0.29$; ◊: $\epsilon = 0.45$; △: $\epsilon = 0.40$). The large difference in utilized capacity between sections △ and ◊ suggests that particle size polydispersity and the associated microstructural inhomogeneities are responsible for the unutilized capacity. In contrast, the galvanostatic response delivered by ◯ suggests an advantageous design as a result of a higher total available active material, in spite of the lower porosity.

Computer-generated microstructures.— In order to systematically quantify the impact of the identified microstructural inhomogeneities on the delivered power and energy density, electrochemical simulations based on DEM generated porous electrodes were performed to complement the microstructural analysis. Figure 8 shows the normalized area density, $a\bar{r}/S_A$, of the reconstructed electrode sections and computer-generated electrodes for different degrees of particle size polydispersity. Calculations show that the area density, i.e., the instantaneous reactivity per unit volume of a battery electrode, approaches the theoretical limit as the polydispersity decreases to zero. In particular, microstructures composed of monodisperse particles allow electrodes to reach the maximal area density of $a\bar{r}/S_A = \pi/\sqrt{2} \approx 2.2$ for $\epsilon = 1 - \pi/3\sqrt{2} \approx 0.26$, only amplified by the effect of roughness. The area density calculated from the reconstructed microstructures indicates that the experimental electrode possesses an area density

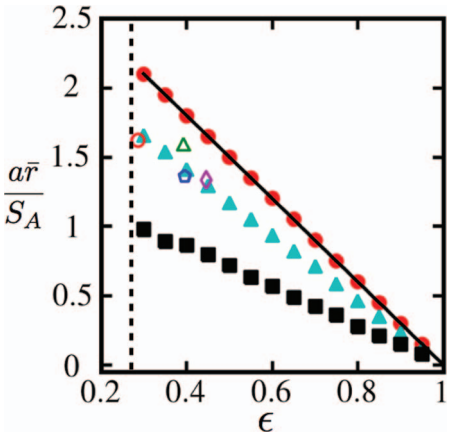

Figure 8. Normalized active surface area per unit volume as a function of porosity. For reconstructed electrode, ⬠ corresponds to the area density of the entire reconstructed electrode, ◯, ◊, and △ corresponds to the area density of individual tomogram sections. For computer-generated electrodes, ● correspond to monodisperse, randomly distributed electrode particles, ▲ to $\sigma_r = 0.4\bar{r}$, and ■ to $\sigma_r = \bar{r}$. The solid line corresponds to the theoretical area density limit. The dash line corresponds to the porosity limit of a crystalline close-packed electrode, $\epsilon = 1 - \pi/3\sqrt{2} \approx 0.26$. The maximum area density is $a\bar{r}/S_A = \pi/\sqrt{2} \approx 2.2$ for an electrode composed of spherical particles exhibiting close-packed configuration.

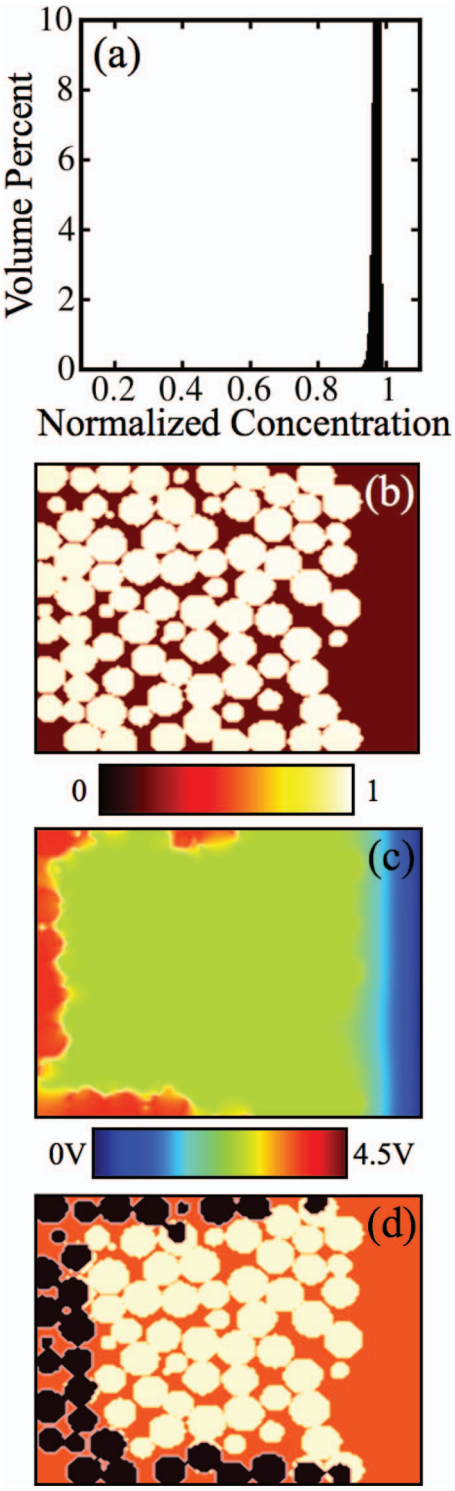

Figure 9. Electrochemical behavior for computer-generated cathode microstructures based on a monodisperse particle size distribution, $\sigma_r = 0$, for a 1C discharge. (a) Lithium concentration histogram, (b) concentration distribution and (c) voltage fields demonstrate that a uniform microstructure results in a uniform electrochemical response. (d) highlights those regions where faster lithium intercalation is favored.

comparable to perfectly spherical particle based electrodes with a polydispersity of $\sigma_r = 0.4\bar{r}$. The area density, however, varies from one section to the next and has a direct impact on the useful capacity.

Figure 9 shows the local electrochemical response of a monodisperse particle size distribution electrode at the end of a 1C discharge.

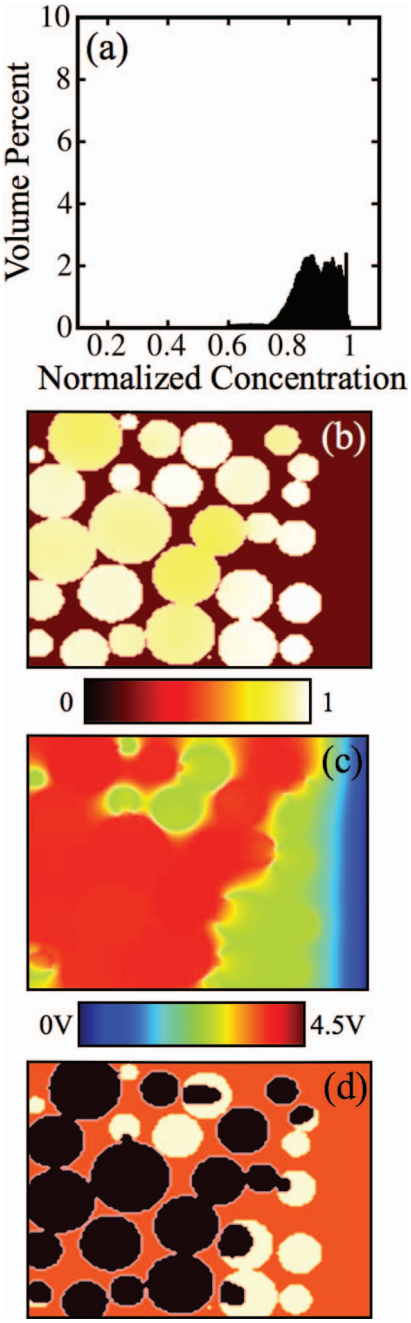

Figure 10. Electrochemical behavior for a computer-generated cathode microstructure based on a polydisperse particle size distribution, $\sigma_r = \bar{r}$, for a 1C discharge. (a) Lithium concentration histogram, (b) concentration distribution and (c) voltage fields show that polydispersity and disorder particle packing result in significant variation in the spatial electrochemical behavior. (d) highlights regions where faster lithium intercalation is favored, and particle packing disorder induces local electrochemical shielding.

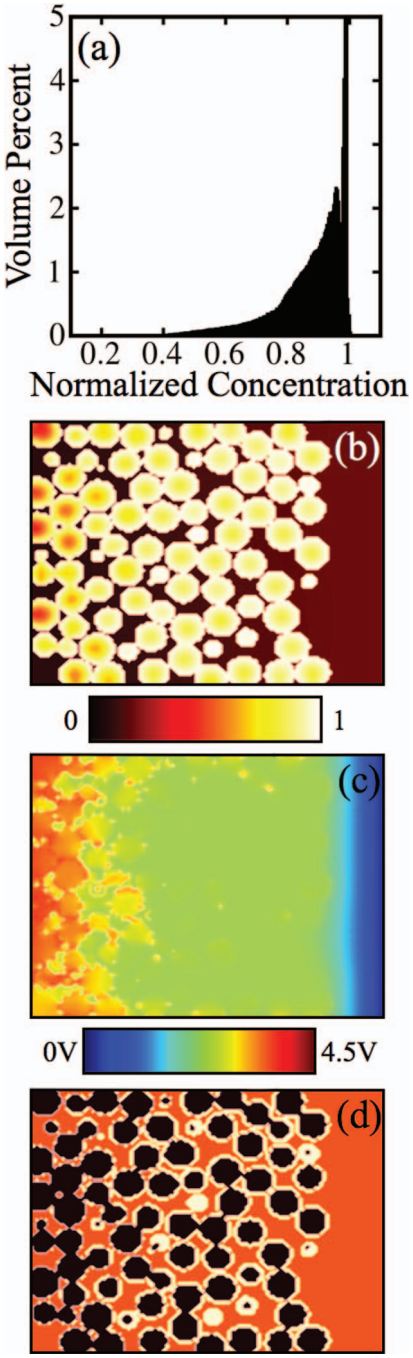

Figure 11. Electrochemical performance of an electrode comprised of a monodisperse distribution of particles, $\sigma_r = 0$, for a very high C-rate, 20C. (a) Macroscopic lithium concentration distribution, (b) spatial concentration, and (c) voltage distributions demonstrate uniform utilization of active material in monodisperse electrodes. (d) highlights the evenly utilized surface of the active material.

The electrode microstructure exhibits a uniform porosity distribution and particle packing. In agreement with the analysis on the experimental microstructure performed herein, microstructurally uniform porous electrodes result in an homogeneous lithium concentration intercalation and voltage distribution.

Figure 10 shows the electrochemical state of an electrode of a polydisperse distribution of particle radii, whose standard deviation is $\sigma_r = \bar{r}$. The resultant chemical and electrical state is shown at the end of a 1C discharge. In contrast to the monodisperse electrode, the polydisperse electrode exhibits microstructural dependent concentration and voltage distribution similar to the one exhibited by the reconstructed experimental microstructure. The local variation in porosity distribution and particle size polydispersity induces local lithium concentration and voltage inhomogeneities. In addition, electrodes that possess a high degree of particle size polydispersity exhibit electrochemical shielding, particularly in those regions that exhibit large particles interacting with smaller ones.

Figure 11 shows that for very high discharge rates, e.g., 20C, the macroscopic power density of an electrode is strongly controlled by the available area density. In this case, a monodisperse particle

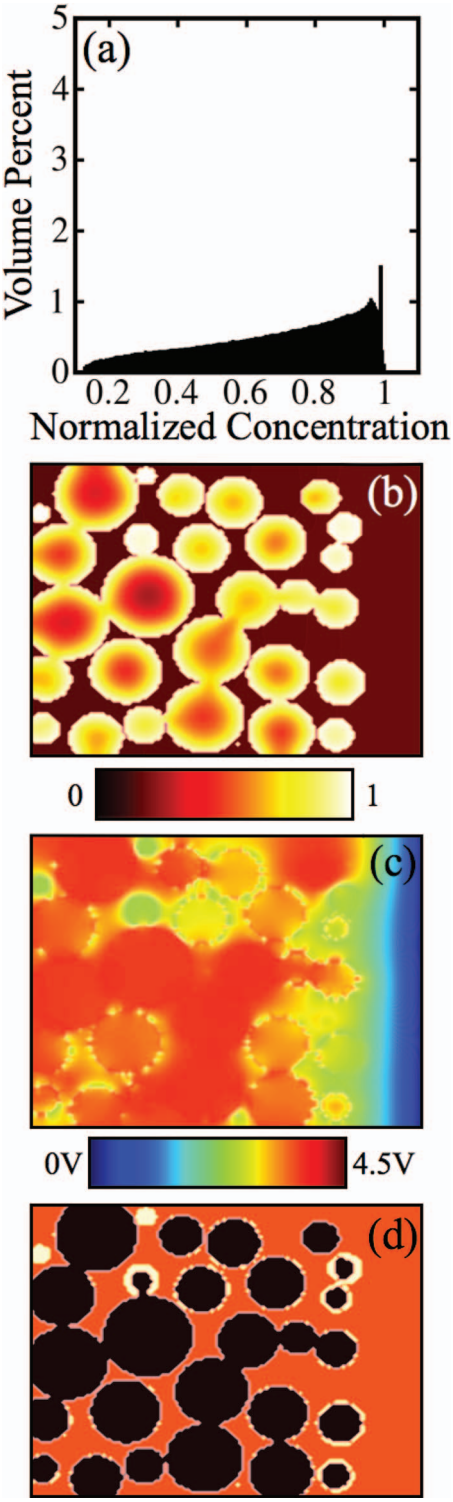

Figure 12. Electrochemical performance of a polydisperse distribution of particles, $\sigma_r = \bar{r}$, for a very high C-rate, 20C. (a) Macroscopic lithium concentration distribution, (b) spatial concentration, and (c) voltage distributions show the electrochemical performance is highly nonuniform, and a significant fraction of the active material is unused. (d) highlights that smaller particles exhibit a faster intercalation rate with respect to larger particles, and shield the larger ones from contributing to performing electrical work.

size electrode microstructure displays a uniform concentration and voltage distribution. Thus, in agreement with area density calculations, Figure 11(d) demonstrates that the surface of active material is highly utilized in the monodisperse electrode.

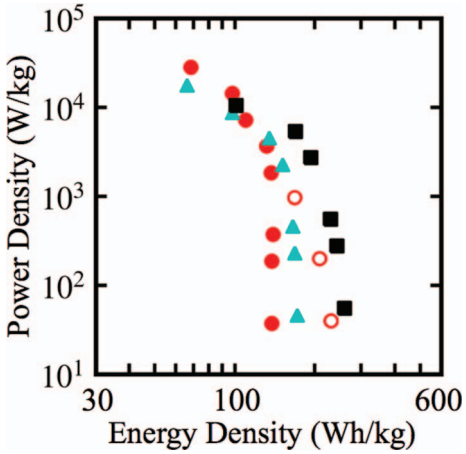

Figure 13. Power density response (Ragone plot) for electrode microstructures for varying degrees of particle size polydispersity. ● correspond to a monodisperse particle size distribution, ▲ corresponds to $\sigma_r = 0.4\bar{r}$, and ■ to $\sigma_r = \bar{r}$. ◯ corresponds to section of experimentally reconstructed electrode. Polydisperse particle size distribution provides a factor of two higher energy density for low and moderate C-rates while the power performance of monodisperse particle size distribution exceeds the performance of a polydisperse size distribution up to a factor of five for high C-rates applications.

Unlike electrode microstructures with a monodisperse distribution of particles, a porous electrode with a degree of polydispersity, $\sigma = \bar{r}$, results in greater spatial inhomogeneities in electric fields, and smaller amounts of utilized active material. In particular, the core of the largest particles remain delithiated at the end of the discharge, see Figure 12. Moreover, result shows that small particles dominate the electrochemical performance for a high C-rate discharge, leaving larger particles unutilized.

Figures 13 summarizes the macroscopic power density response as a function of energy density for electrodes of different degrees of particle size polydispersity. Results show that for polydisperse particle size distributions and low C-rates, a greater energy density is delivered in comparison to monodisperse particle size distributions. Locally, small particles lithiate faster than large particles, thus provide useful instantaneous power while large particles exhibit slower reaction kinetics and a low state of charge. These local particle size differences lead to electrochemical potential gradients between the particles that are annealed out by inducing mass fluxes from the large particles to the neighboring smaller particles which ultimately result in a larger energy density. In contrast, electrodes exhibiting a monodisperse particle size distribution lithiate uniformly and result in a uniform decline in spatial voltage.

At very high discharge rates, however, the power density delivered by a monodisperse particle size distribution electrode performs up to factor of five better than a polydisperse distribution electrode because of the factor of two increase of reaction area per unit volume available for intercalation, in agreement with existing accounts reported literature.[5] Broad particle size distributions impose localized large diffusion distances in the largest particles, and thus result in smaller amounts of utilized charge.

A comparison against the three-dimensionally reconstructed microstructure demonstrates that the particle surface inhomogeneities are detrimental to power density. Here, as the C-rate increases, the different particle size subpopulations become activated and its local electrochemical kinetics are suppressed as a result of the inhomogeneities on particle roughness. Furthermore, in combination with the polarization losses that result from the tortuosity inhomogeneities introduced during electrode compaction,[11] the macroscopic power density of the reconstructed electrode decreases faster than the computer-generated equivalent electrode integrated by a polydisperse particle size distribution.

Conclusions

By using three-dimensional X-ray tomography data of a $LiMn_2O_4$ battery electrode and computer-generated microstructures, the impact of particle size polydispersity, and surface area density on the electrochemical performance of battery electrodes was assessed. Electrochemical simulations show that the reconstructed electrode contains clusters of small particles which induce mesoporous channels that facilitate lithium intercalation. In contrast, regions populated with large particles exhibit a lower lithium intercalation. Results also demonstrate that electrode regions exhibiting a different degree of particle size polydispersity will deliver different amounts of useful charge capacity. Experimentally reconstructed electrodes were found to exhibit a surface area density 2.5 times higher than electrodes made out of perfectly smooth and spherical particles, as assumed by porous electrode theory. The large surface roughness provides a larger instantaneous power density, but also favor an increase in the occurrence of parasitic reactions. Furthermore, mechanical analysis reveals that processing methods that result in interconnected particles will lower the mechanical reliability of the electrode.

Electrochemical simulations show that a factor of two energy density enhancement can be achieved by using polydisperse particle size electrodes for low C-rate applications. Monodisperse electrodes deliver a factor of five higher power density for high discharge rates, due to a higher surface area per volume ratio. Overall, the performed analysis demonstrates that advanced battery designs can be realized by first engineering the particle size polydispersity by customizing it to meet a high power (monodisperse) or high energy density (polydisperse) applications.

Acknowledgments

DWC and REG thank the financial support from National Science Foundation CMMI 0856491. DWC would like to acknowledge the assistance from Dr. David R. Ely on Discrete Element Method simulations. PS is grateful to the Royal Academy of Engineering for financial support, and appreciate Jeff Gelb at Xradia Inc, and Prof. Withers and Dr. Bradley at University of Manchester for X-ray tomographic data collection. NPB thanks EPSRC for financial support.

References

1. S. Chu and A. Majumdar, *Nature*, **488**, 294 (2012).
2. J.-M. Tarascon and M. Armand, *Nature*, **414**, 359 (2001).
3. H. Zhang, X. Yu, and P. V. Braun, *Nature Nanotechnology*, **6**, 277 (2011).
4. W. Lai, C. K. Erdonmez, T. F. Marinis, C. K. Bjune, N. J. Dudney, F. Xu, R. Wartena, and Y.-M. Chiang, *Advanced Energy Materials*, **22**, E139 (2010).
5. M. Smith, R. E. García, and Q. Horn, *Journal of The Electrochemical Society*, **156**, A896 (2009).
6. T. S. Arthur, D. J. Bates, N. Cirigliano, D. C. Johnson, P. Malati, J. M. Mosby, E. Perre, M. T. Rawls, A. L. Prieto, and B. Dunn, *MRS Bulletin*, **36**, 523 (2011).
7. J. W. Long, B. Dunn, D. R. Rolison, and H. S. White, *Chemical Reviews*, **104**, 4463 (2004).
8. A. Vu, Y. Qian, and A. Stein, *Advanced Energy Materials*, **2**, 1056 (2012).
9. M. Ebner, D.-W. Chung, R. E. García, and V. Wood, "Tortuosity Anisotropy in Lithium Ion Battery Electrodes," *Advanced Energy Materials*. Published online.
10. B. Vijayaraghavan, D. R. Ely, Y.-M. Chiang, R. García,-García, and R. E. García, *Journal of The Electrochemical Society*, **159**, A548 (2012).
11. D.-W. Chung, M. Ebner, V. Wood, and R. E. García, *Modelling and Simulation in Materials Science and Engineering*, **21**, 074009 (2013).
12. P. R. Shearing, L. E. Howard, P. S. Jorgensen, N. P. Brandon, and S. J. Harris, *Electrochemistry Communications*, **12**, 374 (2010).
13. D. Kerhwalk, P. R. Shearing, N. P. Brandon, P. K. Sinha, and S. J. Harris, *Journal of The Electrochemical Society*, **158**, A1393 (2011).
14. S. J. Cooper, D. S. Eastwood, J. Gelb, G. Damblanc, D. J. L. Brett, R. S. Bradley, P. J. Withers, P. D. Lee, A. J. Marquis, N. P. Brandon, and P. R. Shearing, "Image Based Modelling of Microstructural Heterogeneity in $LiFePO_4$ Electrodes for Li-ion Batteries," *Journal of Power Sources*, In-press.
15. D. E. Stephenson, B. C. Walker, C. B. Skelton, E. P. Gorzkowski, D. J. Rowenhorst, and D. R. Wheeler, *Journal of The Electrochemical Society*, **158**, A781 (2011).
16. M. Ender, J. Joos, T. Carraro, and E. Ivers-Tiffee, *Electrochemistry Communications*, **13**, 166 (2011).
17. T. Hutzenlaub, S. Thiele, R. Zengerle, and C. Ziegler, *Electrochemical and Solid-State Letters*, **15**, A33 (2012).
18. J. R. Wilson, J. S. Cronin, S. A. Barnett, and S. J. Harris, *Journal of Power Sources*, **196**, 3443 (2011).
19. M. Ebner, F. Geldmacher, F. Marone, M. Stampanoni, and V. Wood, "X-ray Tomography of Porous, Transition Metal Oxide Based Lithium Ion Battery Electrodes," *Advanced Energy Materials*, Published online.
20. M. Doyle and J. Newman, *Electrochimica Acta*, **40**, 2192 (1995).
21. C. M. Doyle, "Design and Simulation of Lithium Rechargeable Batteries," PhD thesis, University of California at Berkeley, Berkeley, CA, 1995.
22. T. M. Fuller, M. Doyle, and J. Newman, *Journal of The Electrochemical Society*, **141**, 1 (1994).
23. P. Arora, M. Doyle, and R. E. White, *Journal of The Electrochemical Society*, **146**, 3543 (1999).
24. R. Darling and J. Newman, *Journal of The Electrochemical Society*, **144**, 3057 (1997).
25. H. Hellweg, "Microstructural Modeling of Lithium Battery Electrodes," MS thesis, Massachusetts Institute of Technology, Cambridge, MA, 2000.
26. W. B. Gu and C. Y. Wang, *Journal of The Electrochemical Society*, **147**, 2910 (2000).
27. W. B. Gu and C. Y. Wang, *Journal of The Electrochemical Society*, **147**, 427 (2000).
28. L. Rao and J. Newman, *Journal of The Electrochemical Society*, **144**, 2697 (1997).
29. L. Song and J. W. Evans, *Journal of The Electrochemical Society*, **147**, 2086 (2000).
30. K. E. Thomas and J. Newman, *Journal of The Electrochemical Society*, **150**, A176 (2003).
31. G. G. Botte, V. R. Subramanian, and R. E. White, *Electrochimica Acta*, **45**, 2595 (2000).
32. G. G. Botte and R. E. White, *Journal of The Electrochemical Society*, **148**, A54 (2001).
33. R. E. García and Y.-M. Chiang, *Journal of The Electrochemical Society*, **159**, A856 (2007).
34. R. E. García, Y.-M. Chiang, W. C. Carter, P. Limthongkul, and C. M. Bishop, *Journal of The Electrochemical Society*, **152**, A255 (2005).
35. A. Gupta, J. H. Seo, X. Zhang, W. Du, A. M. Sastry, and W. Shyy, *Journal of The Electrochemical Society*, **158**, A487 (2011).
36. X. Zhang, W. Shyy, and A. M. Sastry, *Journal of The Electrochemical Society*, **154**, A910 (2007).
37. X. Zhang, A. M. Sastry, and W. Shyy, *Journal of The Electrochemical Society*, **155**, A542 (2008).
38. B. Yan, C. Lim, L. Yin, and L. Zhu, *Journal of The Electrochemical Society*, **159**, A1604 (2012).
39. A. H. Wiedemann, G. M. Goldin, S. A. Barnett, H. Zhu, and R. J. Kee, *Electrochimica Acta*, **88**, 580 (2013).
40. R. E. García, C. M. Bishop, and W. C. Carter, *Acta Materialia*, **52**, 11 (2004).
41. D.-W. Chung, N. Balke, S. V. Kalinin, and R. E. García, *Journal of The Electrochemical Society*, **158**, A1083 (2011).
42. J. Newman, *Electrochemical Systems*, Prentice Hall International, Englewood Cliffs, NJ, USA (1980).
43. J. F. Nye, *Physical Properties of Crystals, Their Representation by Tensors and Matrices*, Oxford University, London, United Kingdom (1998).
44. P. R. Shearing, N. P. Brandon, J. Gelb, R. Bradley, P. J. Withers, A. J. Marquis, S. Cooper, and S. J. Harris, *Journal of The Electrochemical Society*, **159**, A1012 (2012).
45. S. Abe, C. Altinay, V. Boros, W. Hancock, S. Latham, P. Mora, D. Place, W. Petterson, Y. Wang, and D. Weatherley, ESyS-Particle: HPC Discrete Element Modeling Software. Published: Open Software License version 3.0 (2009).
46. B. Vijayaraghavan, R. E. García, and Y.-M. Chiang, *219th ECS Meeting*, MA2011-01, May 1-May 6, 2011, Montreal, QC, Canada, B5 - Microstructure, Mechanisms, and Modeling of Battery Materials.
47. A. J. Izenman, *Journal of the American Statistical Association*, **86**, 205 (1991).
48. S. J. Harris, R. D. Deshpande, Y. Qi, I. Dutta, and Y.-T. Cheng, *Journal of Materials Research*, **25**, 1433 (2010).
49. O. Keles, R. E. García, and K. J. Bowman, *Acta Materialia*, **61**, 2853 (2013).
50. T. Ohzuku, H. Tomura, and K. Sawai, *Journal of The Electrochemical Society*, **144**, 3496 (1997).
51. Y. Itou and Y. Ukyo, *Journal of Power Sources*, **146**, 39 (2005).
52. W. H. Woodford, Y.-M. Chiang, and W. C. Carter, *Journal of The Electrochemical Society*, **157**, A1052 (2010).
53. T. Ohzuku, S. Kitano, M. Iwanaga, H. Matsuno, and A. Ueda, *Journal of Power Sources*, **68**, 646 (1997).
54. G. G. Amatucci, C. N. Schmutz, A. Blyr, C. Sigala, A. S. Gozdz, D. Larcher, and J. M. Tarascon, *Journal of Power Sources*, **69**, 11 (1997).